Available online at www.sciencedirect.com
ScienceDirect
Trans. Nonferrous Met. Soc. China 34(2024) 2491−2506
Transactions of Nonferrous Metals Society of China
www.tnmsc.cn

Effect of addition temperature on dispersion behavior and grain refinement efficiency of MgO introduced into Mg alloy

Le ZAI[1], Xin TONG[1], Yun WANG[2], Xiao-huai XUE[1]

1. School of Materials Science and Engineering, Shanghai Jiao Tong University, Shanghai 200240, China;
2. Brunel Centre for Advanced Solidification Technology (BCAST), Brunel University London, Uxbridge, Middlesex UB8 3PH, United Kingdom

Received 22 February 2023; accepted 12 October 2023

Abstract: The effect of addition temperature of MgO particles (MgO_p) on their dispersion behavior and the efficiency of grain refinement in AZ31 Mg alloy was investigated. In addition, the grain refinement mechanism was systematically studied by microstructure characterization, thermodynamic calculation, and analysis of solidification curves. The results show that the grain size of AZ31 Mg alloy initially decreases and then increases as the MgO_p addition temperature is increased from 720 to 810 °C, exhibiting a minimum value of 136 μm at 780 °C. The improved grain refinement efficiency with increasing MgO_p addition temperature can be attributed to the reduced Mg melt viscosity and enhanced wettability between MgO_p and Mg melt. Furthermore, a corresponding physical model describing the solidification behavior and grain refinement mechanism was proposed.

Key words: grain refinement; MgO nucleation particles; AZ31 alloy; addition temperature; dispersion behavior

1 Introduction

Grain refinement is a crucial technique to simultaneously promote the mechanical properties and castability of Mg−Al series alloys. Currently, the grain refinement techniques for Mg−Al alloys primarily involve mico-alloying with high Q values (e.g. Ti, Sr) [1,2] and carbon inoculation [3−5]. However, the micro-alloying method alters the alloy composition, and the generation of heterogeneous nuclei Al_4C_3 during carbon inoculation is susceptible to poisoning by Fe/Mn elements [5,6], leading to a degradation in grain refinement.

In recent years, there has been increasing attention on the use of metal oxides as effective grain refiners for Mg and its alloys [7−11]. Among them, MgO has been identified as an effective heterogeneous nucleation particle for Mg−Al alloys [10,11]. Compared with other heterogeneous particles, MgO exhibits superior thermal stability. Additionally, its fading effect on grain refinement is relatively lower, which can be attributed to the smaller density difference compared to Mg. FAN et al [12] applied a strong shearing process to the AZ91D alloy melt, resulting in a significant reduction in grain size. It was concluded that the shearing process broke the oxide film into MgO particles (MgO_p), thereby increasing the nucleation sites for α-Mg grains. MA et al [11] systematically investigated the effects of MgO_p addition amount and holding time on the grain refinement efficiency of Mg−Al alloys. Experimental results revealed that the optimal addition amount of MgO_p and holding time were approximately 1.5% and 10 min, respectively. The grain refinement mechanism is attributed to the formation of $MgAl_2O_4$, which serves as effective nucleation sites for α-Mg grains

Corresponding author: Xiao-huai XUE, Tel: +86-13166330878, E-mail: xhxue@sjtu.edu.cn
DOI: 10.1016/S1003-6326(24)66555-6

through the reaction of Al with MgO_p.

Due to the large specific surface area and high surface energy of particles, MgO_p is easily agglomerated in the Mg melt. It is widely acknowledged that the efficiency of grain refinement is closely related to the distribution of heterogeneous nuclei during the initial nucleation stage [13]. In the study of composites fabricated by stirring casting [14−16], the stirring temperature is a crucial process parameter that affects the distribution of particles. The temperature significantly impacts the thermal and physical parameters (such as surface tension and viscosity) of the alloy melt, which, in turn, has a significant influence on the distribution of added particles in the melt. During the fabrication process of metal matrix composites reinforced with particles (such as Al−SiC [17], Al−MgO [18], and Mg−SiC [19]) via stirring casting, it has been observed that there exists an optimal addition temperature for achieving a homogeneous dispersion of these particles.

Previous studies [11] have shown that the reaction of MgO_p with Al leads to the formation of $MgAl_2O_4$. Therefore, the temperature not only influences the distribution of MgO_p in the Mg melt but also affects the metallurgical reaction rate between MgO_p and Al. Moreover, the wettability of the melt on the surface of heterogeneous nuclei plays a crucial role in heterogeneous nucleation [20]. All of these factors are temperature-dependent, thereby impacting the grain refinement efficiency. Existing studies on grain refinement of Mg−Al alloys using MgO_p have primarily focused on the addition mode (external method [11] and in-situ formation [10,12,21]), as well as the effects of addition amount and holding time on grain refinement efficiency [11]. However, the effect of the MgO_p addition temperature on the grain refinement efficiency of Mg−Al alloys has not been investigated. Given these circumstances, it is essential to study the effect of MgO_p addition temperature on grain refinement and conduct further in-depth research.

In this study, we investigated the impact of the MgO_p addition temperature on its dispersion behavior and grain refinement efficiency. The metallurgical reaction between MgO_p and the AZ31 Mg alloy melt, as well as the effect of the MgO_p addition temperature on the mechanical properties, was also discussed.

2 Experimental

The AZ31 Mg alloys were prepared using pure Mg (99.98 wt.%), pure Al (99.99%), and pure Zn (99.99%) in an electrical resistance furnace with N_2 + 1% SF6 (volume fraction) mixed atmosphere as a protective measure. The raw materials were melted, and the temperature was maintained at 740 °C for 10 min to achieve the complete composition homogenization. For the purification of the alloy, the melt was flux-refined using a refining agent. After removing the oxide skin, MgO particles (1.2%) wrapped in aluminum foils were introduced into the melt at 720 °C. The average particle size of MgO is approximately 1.03 μm, as shown in Fig. 1. Subsequently, the stirring blade was activated at a rotation speed of 60 r/min for 5 min to ensure uniform distribution of MgO_p. The addition temperature of MgO_p was set to be 720, 750, 780 and 810 °C, respectively. For comparison, an AZ31 Mg alloy without MgO_p addition was also prepared under identical processing conditions, including the stirring process. Finally, samples for testing grain size were ladled out using a steel ladle (d30 × d20 × 25 mm, wall thickness 2.2 mm) and directly solidified within the ladle. It is important to note that the melt surface was monitored, and the casting process was carried out promptly when MgO particles were not visible on the surface of the melt. Maintaining the same sampling temperature ensured that all samples solidified at the same cooling rate, thereby eliminating the influence of the cooling rate on grain refinement. The cooling curve was recorded using a computer-aided cooling curve analysis (CA-CCA) system with a time step of 0.5 s. The alloy compositions of the obtained casting samples were determined by Inductively Couple Plasma-Atomic Emission Spectroscopy (ICP-AES) (Table 1).

Metallographic specimens were obtained by sectioning the ingots at a distance of 20 mm from the bottom. These specimens were then mechanically ground, polished, and etched in an acetic-picric solution (consisting of 4.2 g picric acid, 10 mL acetic acid, 10 mL water, and 70 mL ethanol) for 10 s. Phase identification was performed using an X-ray diffractometer (XRD, D8 ADVANCE Da Vinci) with a scanning rate of 2 (°)/min. Detailed morphological characteristics and elemental

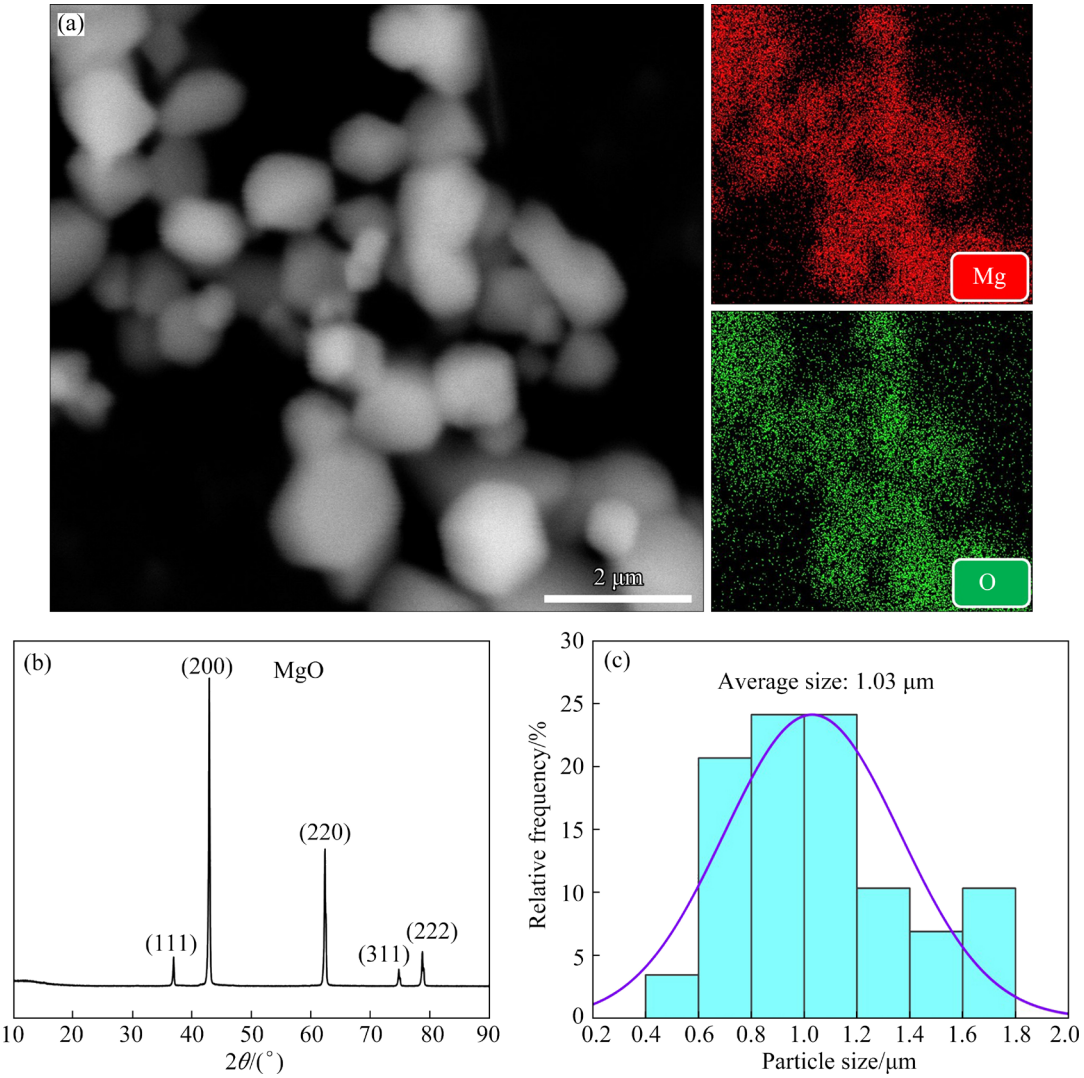

Fig. 1 Structural results of MgO_p: (a) Morphology; (b) XRD pattern; (c) Particle size distribution

Table 1 Actual compositions of studied alloys analyzed by ICP-AES

Sample	Addition temperature of MgO_p/°C	Content/wt.%		
		Al	Zn	Mg
AZ31	–	3.08	1.09	Bal.
AZ31+ 1.2%MgO	720	3.12	1.10	Bal.
	750	3.15	1.12	Bal.
	780	3.11	1.05	Bal.
	810	3.06	1.07	Bal.

distribution were examined using a field-emission scanning electron microscope (SEM, NOVA Nano SEM 230) equipped with an energy-dispersive spectroscope (EDS). Electron back-scattered diffraction (EBSD) was also conducted on the SEM at 20 kV with a step size of 1 μm. The average grain sizes were measured using the linear intercept method (ASTM 112−10). 3D tomographic images were obtained using an X-ray microscope (XRM, Xradia 520 Versa) at 60 kV and 5 W. The data files containing three-dimensional information were processed using Dragonfly software. The morphology, crystal structure, and orientation of the heterogeneous nucleation particles were identified by a high-resolution transmission electron microscopy (HRTEM, Talos F200X G2) operated at 200 kV. Foils with a diameter of 3 mm for HRTEM studies were first punched, ground to a thickness of approximately 40 μm, and then further thinned using the precision ion polishing system (GATAN PIPS II 695).

The tensile properties of these alloys were obtained at room temperature using a tensile testing machine (Zwick/Roell Z100) with a strain rate of 1 mm/min. Three samples were tested for each

alloy to avoid random error. A thermodynamic analysis software, FactSage 8.1, was used to analyze the reaction process of MgO_p subjected to AZ31 Mg alloy melt.

3 Results

3.1 Microstructure analysis

The microstructure of the cast AZ31 Mg alloy without MgO_p addition consists of well-developed α-Mg dendrites surrounded by β-$Mg_{17}Al_{12}$ secondary phases, as depicted in Fig. 2(a). The average grain size of the α-Mg matrix is approximately 400 μm. Notably, serious agglomeration of the MgO_p, approximately 100 μm in size, can be observed along the grain boundaries (GBs) when the addition temperature of MgO_p powder is 720 °C. However, as the addition temperature of MgO_p increases from 720 to 810 °C, a gradual decrease in grain size is observed, as illustrated in Figs. 2(b−e). Moreover, both the number and size of the MgO agglomeration decrease with the increase of the addition temperature.

EBSD was conducted to reveal the GBs for grain size measurement, as shown in Fig. 3. The average grain size of untreated AZ31 Mg alloy is approximately 400 μm. As the MgO_p addition temperature increased from 720 to 810 °C, the average grain sizes of the AZ31 Mg alloy were approximately 324, 243, 136 and 168 μm, respectively, as plotted in Fig. 3(f). Among them, the AZ31 Mg alloy with MgO_p addition at 780 °C exhibits the finest grain size, which is about 58% smaller than that of the untreated alloy.

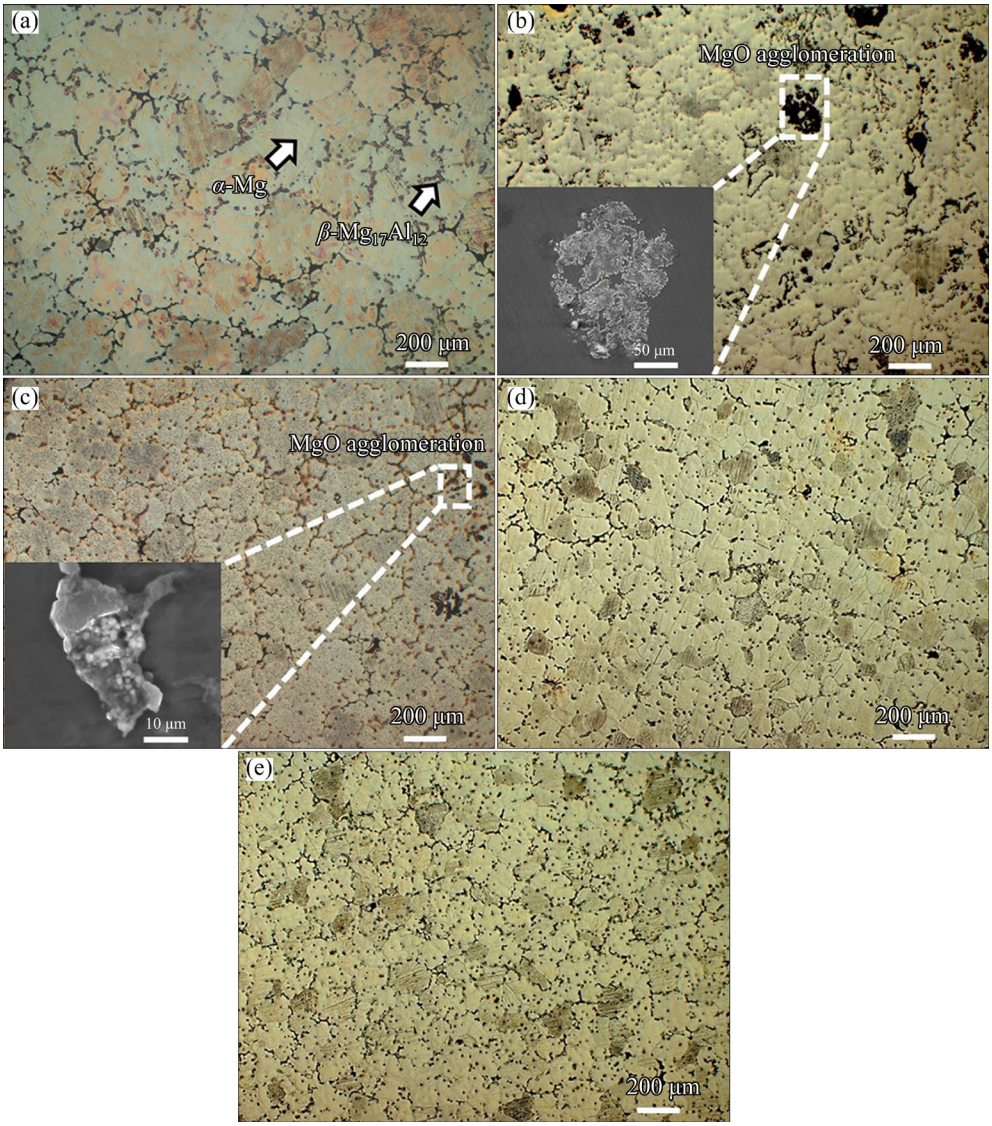

Fig. 2 Optical images of cast AZ31 Mg alloy without MgO_p addition (a) and with MgO_p addition at different temperatures (b−e): (b) 720 °C; (c) 750 °C; (d) 780 °C; (e) 810 °C

Figure 4 shows the microstructure of the studied alloys, where both lamellar eutectic structure and divorced eutectic β-$Mg_{17}Al_{12}$ are observed along the GBs. Serious agglomeration of MgO_p is observed in the AZ31 Mg alloy with MgO_p addition at 720 °C, aligning with the observations through optical microscopy in Fig. 2(b). Furthermore, increasing the MgO_p addition temperature results in a morphological transformation of β-$Mg_{17}Al_{12}$ from a continuous network to a bulk structure.

3D tomography analyses were performed in Fig. 5 to evaluate the effect of the MgO_p addition temperature on the morphology and distribution of β-$Mg_{17}Al_{12}$ and MgO_p. Figures 5(a) and (b) display the reconstruction map of the AZ31 Mg alloy with MgO_p addition at 720 and 780 °C, respectively. Moreover, the morphology and distribution of

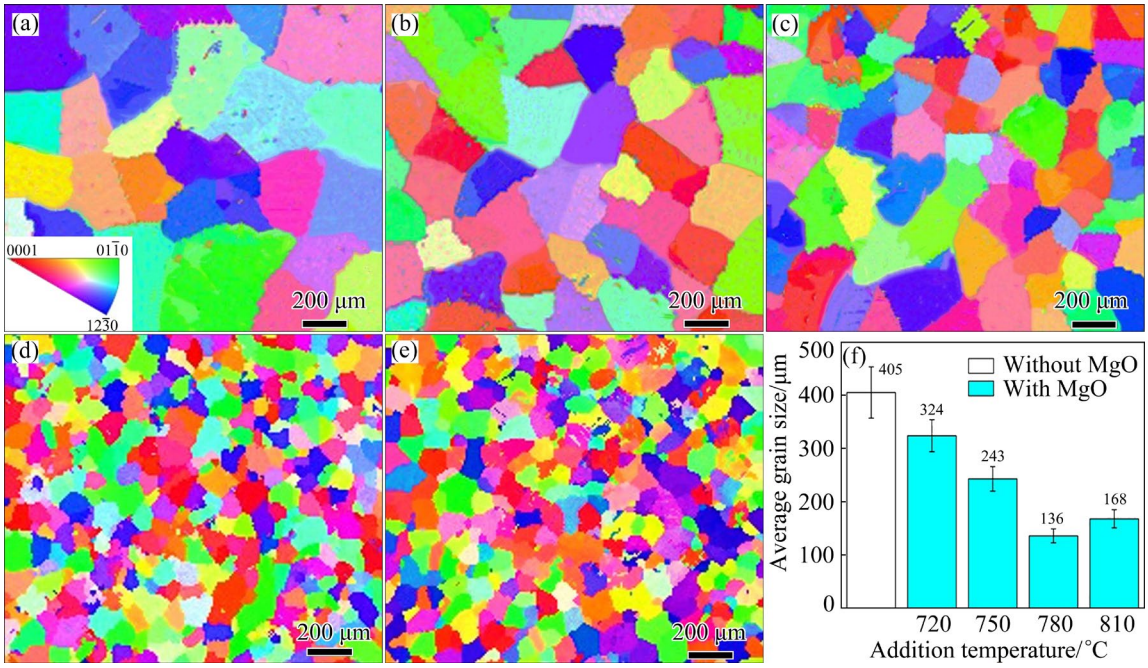

Fig. 3 EBSD analysis results of cast AZ31 Mg alloy without MgO addition (a) and with MgO_p addition at different temperatures (b−e): (b) 720 °C; (c) 750 °C; (d) 780 °C; (e) 810 °C; (f) Effect of addition temperature on grain size

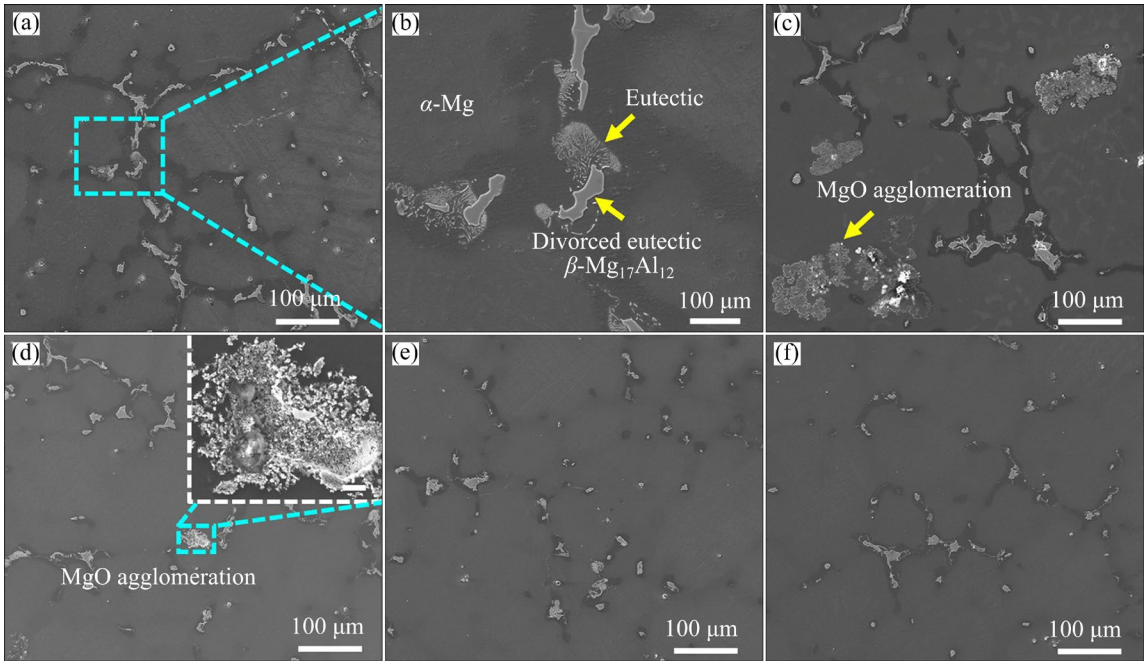

Fig. 4 SEM images of cast AZ31 Mg alloy without MgO addition (a, b) and with MgO_p addition at different temperatures (c−f): (c) 720 °C; (d) 750 °C; (e) 780 °C; (f) 810 °C

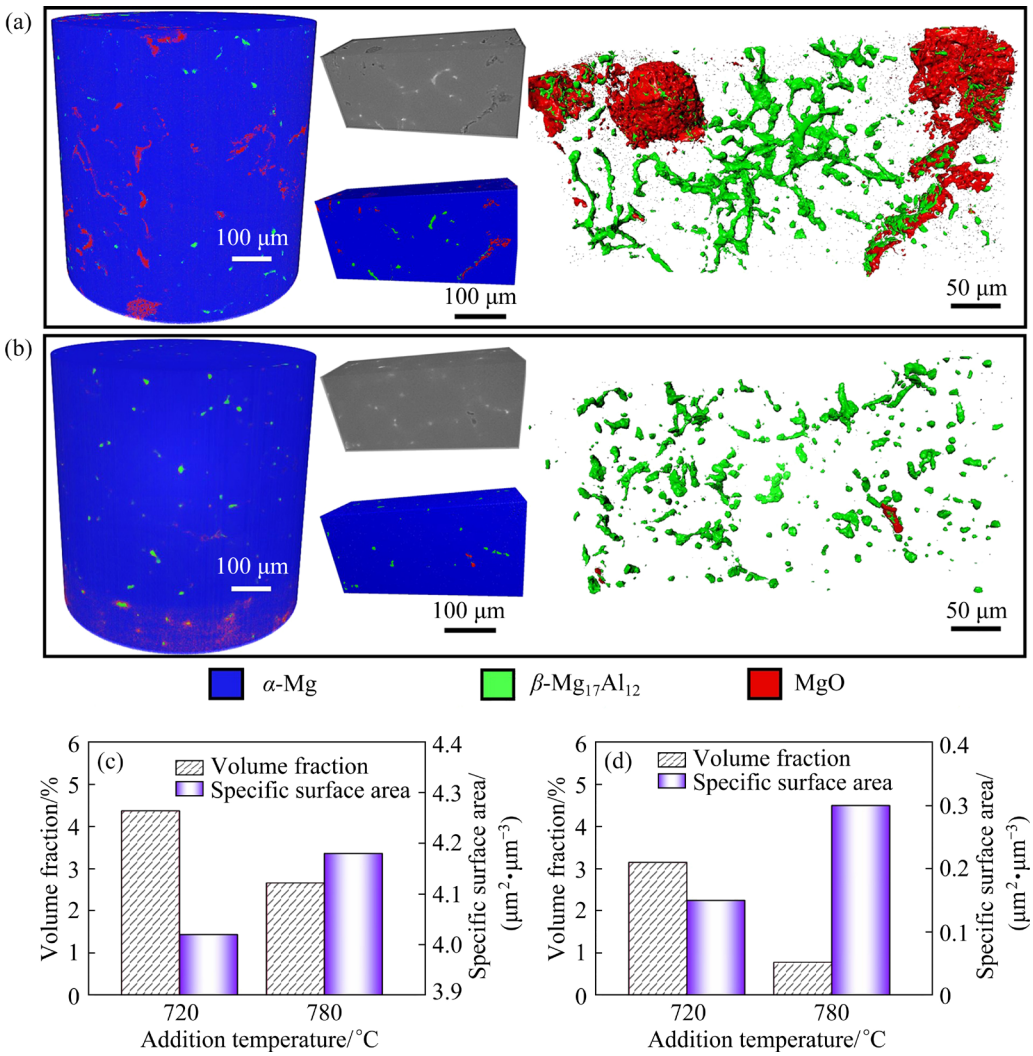

Fig. 5 3D XRM image of cast AZ31 Mg alloy with MgO_p addition at 720 °C (a) and 780 °C (b), and volume fraction and specific surface area of β-$Mg_{17}Al_{12}$ (c) and MgO_p (d), respectively

β-$Mg_{17}Al_{12}$ and MgO_p are also extracted from the cuboid reconstruction map. The continuous three-dimensional network structure of β-$Mg_{17}Al_{12}$ is surrounded by MgO_p agglomerations in the AZ31 Mg alloy with MgO_p addition at 720 °C. However, in the AZ31 Mg alloy with MgO_p addition at 780 °C, β-$Mg_{17}Al_{12}$ is refined and more dispersed. The size of the MgO_p agglomerations is significantly reduced at higher MgO_p addition temperatures. Figures 5(c) and (d) provide quantitative results regarding the volume fraction and specific surface area of β-$Mg_{17}Al_{12}$ and MgO_p in the AZ31 Mg alloy with MgO_p addition at 720 and 780 °C, respectively. It can be observed that the volume fraction of both β-$Mg_{17}Al_{12}$ and MgO_p decreases with increasing MgO_p addition temperature, while their specific surface area exhibits the opposite trend. The volume fraction of MgO_p is also dramatically reduced in the AZ31 Mg alloy with MgO_p addition at 780 °C, which can be attributed to the fact that dispersed MgO_p with smaller sizes cannot be detected by the X-ray microscope due to its limited voxel resolution.

The microstructure of the AZ31 Mg alloy with MgO_p addition at 720 °C is characterized by SEM, as shown in Fig. 6. Figures 6(a–c) display the presence of large-sized MgO aggregates (~50 μm) and the agglomeration of multiple particles. Based on the atomic ratio of Mg to O at Point 1, the particles observed in Fig. 6(b) are likely to be MgO_p. Furthermore, MgO_p is also observed within the grain interior, suggesting the occurrence of heterogeneous nucleation during solidification with the addition of MgO_p, as shown in Fig. 6(c).

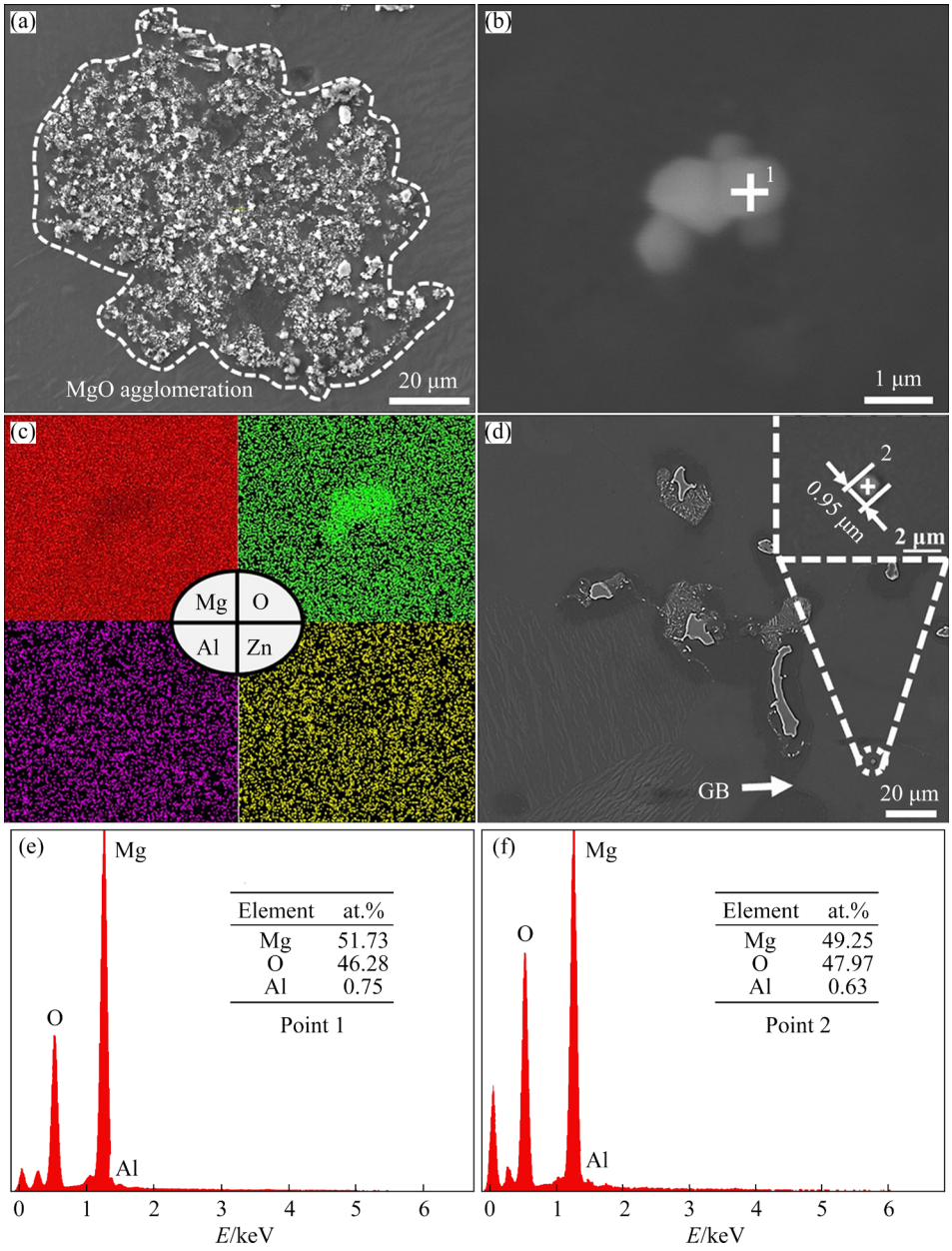

Fig. 6 SEM images of cast AZ31 Mg alloy with MgO addition at 720 °C: (a) Large agglomerated MgO_p; (b) Several agglomerated MgO_p; (c) EDS mapping of (b); (d) Single dispersed MgO_p within grain; (e, f) EDS analysis of Points 1 and 2, respectively

Selected-area electron diffraction (SAED), HRTEM lattice, and EDS images were utilized to determine the crystal structure and elements of the particles. Figure 7 provides TEM images of the AZ31 Mg alloy with MgO_p addition at 780 °C. Figure 7(a) shows a TEM bright-field image depicting the morphology of the MgO_p agglomeration. The single dispersed MgO_p is visible in the TEM high-angle annular dark field image (HAADF). The MgO_p retains its original morphology, and good interfacial bonding between MgO and the Mg matrix is visible. Based on the EDS point analysis (Fig. 7(c)) and SAED spectrum (Fig. 7(e)), the particle within the α-Mg matrix can be identified as MgO_p. The SAED pattern gives an experimental lattice parameter, with a value of a=0.4207 nm for the MgO in this study. This value is comparable to the reported room temperature value of a=0.42112 nm for MgO found in the literature [22]. To investigate the role of MgO_p in the nucleation of α-Mg during the solidification process, the orientation relationship between MgO_p and the surrounding α-Mg matrix was analyzed, as shown in Fig. 7(f).

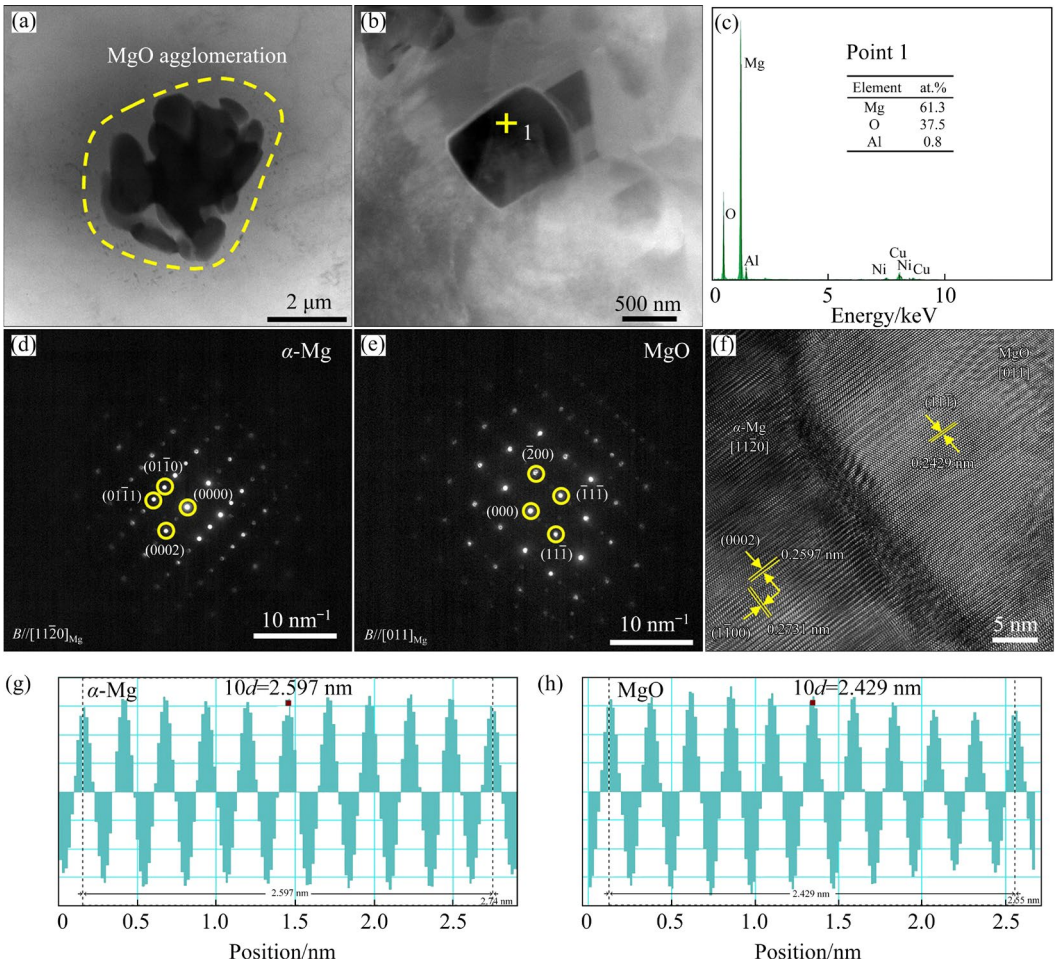

Fig. 7 TEM images of cast AZ31 Mg alloy with MgO_p addition at 780 °C: (a) TEM bright-field image showing morphology of agglomerated MgO_p; (b) HAADF image showing morphology of single dispersed MgO_p; (c) EDS point analysis; (d, e) SAED patterns of α-Mg and MgO; (f) HRTEM image showing interface between MgO_p and α-Mg matrix; (g, h) Frame profiles of average fringe width of $(0002)_{\alpha\text{-Mg}}$ and $(111)_{MgO}$ crystallographic plane, respectively

The thin foil was tilted to align the incident beam parallel to the $[11\bar{2}0]_{\alpha\text{-Mg}}$ zone axis direction, while the MgO was orientated along its $[01\bar{1}]$ direction. This reveals that $[11\bar{2}0]_{\alpha\text{-Mg}}$ is parallel to $[01\bar{1}]_{MgO}$, and the α-Mg presents the orientation relations of $[11\bar{2}0]_{\alpha\text{-Mg}}//[01\bar{1}]_{MgO}$ and $(0002)_{\alpha\text{-Mg}}//(111)_{MgO}$ with MgO. Figures 7(g, h) show the frame profiles of the average fringe width for the $(0002)_{\alpha\text{-Mg}}$ and $(111)_{MgO}$ crystallographic plane, respectively. The interplanar spacings of the $(0002)_{\alpha\text{-Mg}}$ and $(1\bar{1}00)_{\alpha\text{-Mg}}$ planes were measured to be 0.2597 and 0.2731 nm, respectively. Compared to the reported lattice parameters a=0.32092 nm and c=0.52105 nm for pure Mg at 25 °C [23], the experimental values of a=0.3147 nm and c=0.5194 nm are found to be in good agreement with the α-Mg matrix obtained by measuring d-spacings for $(0002)_{\alpha\text{-Mg}}$ and $(1\bar{1}00)_{\alpha\text{-Mg}}$ using HRTEM lattice images. The unit cell of the α-Mg (Mg−Al−Zn solid solution) exhibits a slight contraction in both the a-axis and c-axis compared to pure Mg. This reduction in lattice parameters is caused by the substitutional Al and Zn atoms in the HCP Mg lattice.

3.2 Mechanical properties and fracture characteristics

The tensile tests were conducted to investigate the effect of MgO_p addition temperature on the tensile properties of the studied alloys, as shown in Fig. 8(a). The tensile properties, including yield strength (YS), ultimate tensile strength (UTS), and elongation (EL) of the alloys are shown in Fig. 8, as a function of the MgO_p addition temperature. The untreated AZ31 Mg alloy exhibits a YS of 44.8 MPa, UTS of 117 MPa, and EL of 9.8%. The

MgO_p addition temperature has a significant effect on the tensile properties of the studied alloys. With increasing MgO_p addition temperature, the UTS initially increases from 70.6 MPa (at 720 °C) to 153.4 MPa (at 780 °C), and then decreases to 144.5 MPa (at 810 °C). The YS values follow a similar trend. The EL of the AZ31 Mg alloy with MgO_p addition at 720 °C is only 3.3%, significantly lower than that of the untreated alloy. However, the EL of the AZ31 Mg alloy with MgO_p addition at 810 °C increases to 11.3%.

Figure 9 shows the tensile fracture characteristics of the studied alloys. The fracture surface of the untreated AZ31 Mg alloy exhibits a

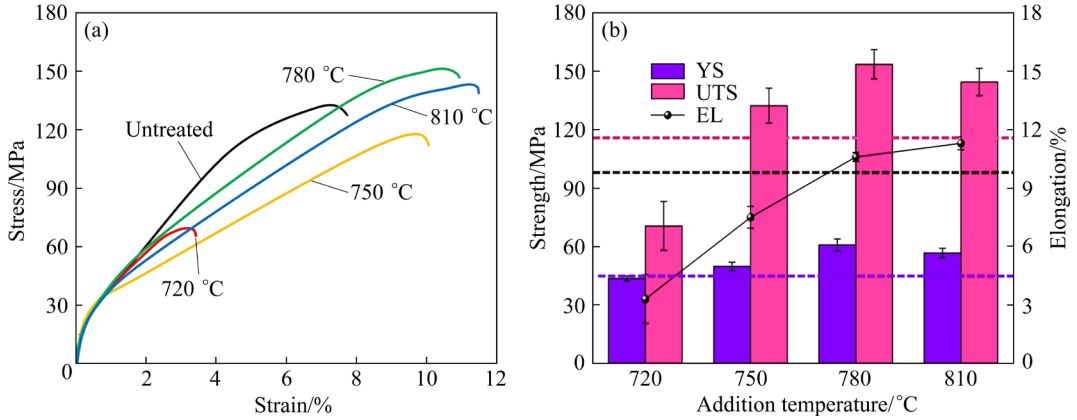

Fig. 8 Mechanical properties of cast AZ31 Mg alloy with MgO_p addition at different temperatures: (a) Stress−strain curve; (b) Tensile property

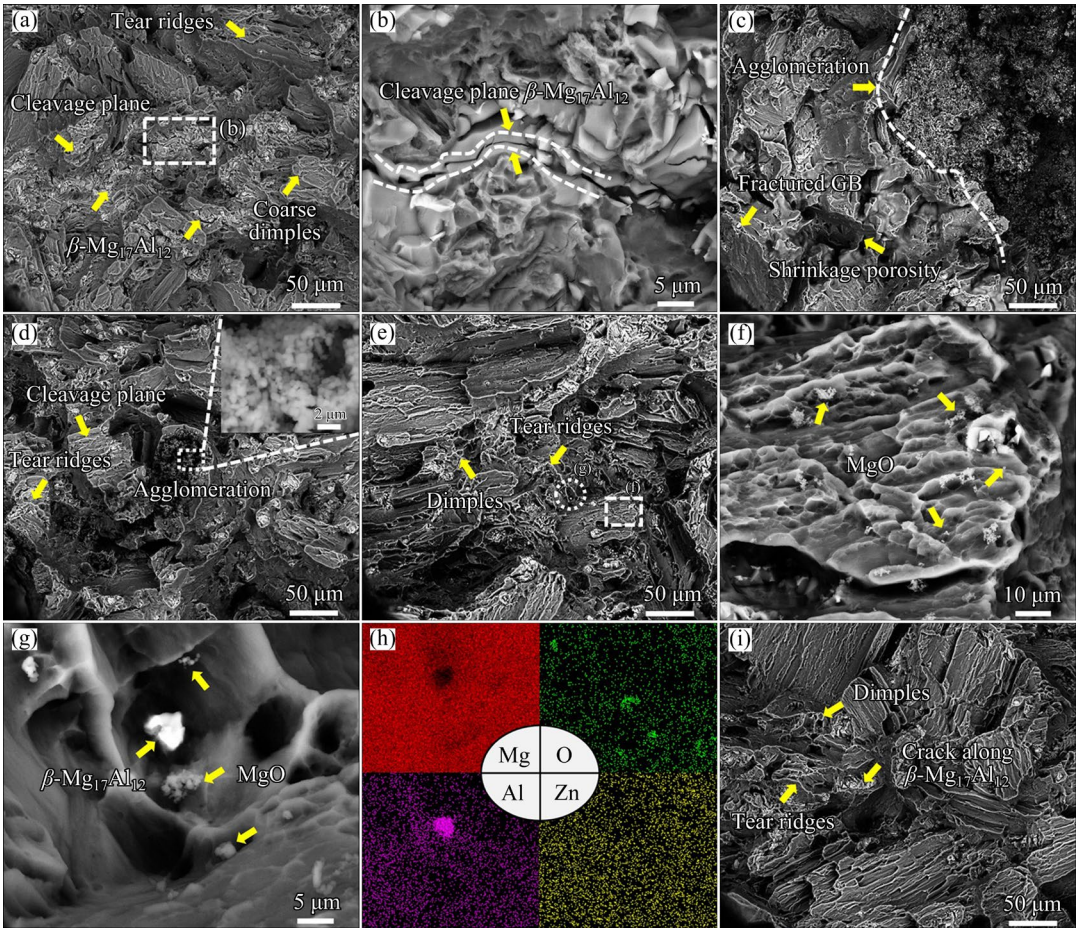

Fig. 9 SEM images of tensile fracture of cast AZ31 Mg alloy without MgO_p addition (a, b) and with MgO_p addition at different temperatures (c−i): (c) 720 °C; (d) 750 °C; (e) 780 °C, (f, g) Local magnified views of (e); (h) EDS mapping of (g); (i) 810 °C

mixed characteristic of transgranular and intergranular fractures. The fracture surface reveals fractured β-$Mg_{17}Al_{12}$, coarse dimples, and cleavage planes, indicating a quasi-cleavage fracture. A large amount of MgO_p can be observed on the fracture surface of the AZ31 Mg alloy with MgO_p addition at 720 °C, indicating that the MgO_p agglomeration acts as inclusions that negatively deteriorate the mechanical properties. The presence of shrinkage pores near the MgO_p agglomeration contributes to the lowest elongation of 3.3%, suggesting that the MgO_p agglomeration reduces the feeding capacity of the alloy during the solidification process. As shown in Fig. 9(d), both the size and amount of the MgO_p agglomeration exposed in the fracture of the AZ31 Mg alloy with MgO_p addition at 750 °C decrease. The fracture surfaces of the AZ31 Mg alloy with MgO_p addition at 780 and 810 °C show the main fracture characteristic of quasi-cleavage, containing coarse dimples and tear ridges. Fine and dispersed MgO_p and β-$Mg_{17}Al_{12}$ can also be found in the fracture under higher magnification (Figs. 9(f) and (g)).

4 Discussion

It is widely recognized that grain refinement in cast metals can be achieved through both heterogeneous nucleation and constitutional supercooling [24,25]. In this study, grain refinement is achieved by the addition of MgO_p without altering the alloy composition. It is worth noting that the stirring speed employed in this study is only 60 r/min, which is significantly lower than the shear speed (500−800 r/min) necessary to break the MgO film into MgO_p during melt shearing process [12]. Therefore, the formation of in-situ MgO_p through the stirring process is not considered. The grain refinement mechanism should be discussed based on the heterogeneous nucleation of α-Mg grains induced by MgO_p.

4.1 Grain refinement mechanism

A previous study [11] found that MgO_p can undergo a reaction with Al in the Mg melt, resulting in the formation of $MgAl_2O_4$ according to the following reaction:

$$4MgO(s)+2Al(l)=MgAl_2O_4(s)+3Mg(l) \quad (1)$$

The Gibbs free energy change (ΔG_T) and enthalpy change (ΔH_T) of Reaction (1) were calculated by the thermodynamic calculation software FactSage 8.1, as shown in Fig. 10. The positive values of ΔG_T and ΔH_T indicate that Reaction (1) is thermodynamically unfavorable. Consequently, the generation of $MgAl_2O_4$ through the reaction of MgO_p with Al is unlikely to occur.

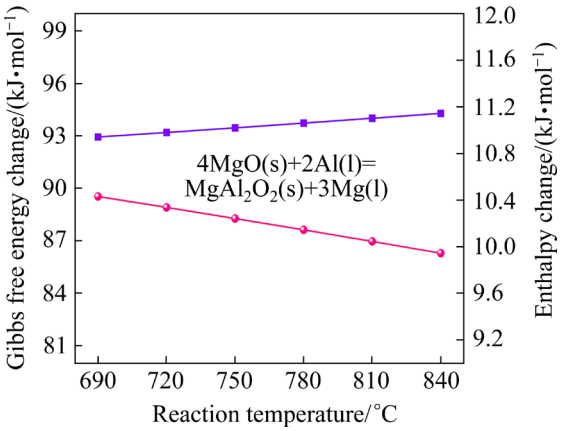

Fig. 10 Thermodynamic calculations of possible reactions after introducing MgO_p into melt

Based on the classic heterogeneous nucleation theory [24,26], particles act as potent heterogeneous nuclei on the premise of low crystallographic disregistry with the matrix and sufficient undercooling for grain nucleation. For the crystallographic disregistry, the orientation relationship (OR) between α-Mg and MgO can be evaluated by an HRTEM lattice image. There is a potential matching relationship between α-Mg and MgO with the OR of $\langle 11\bar{2}0\rangle_{Mg}//\langle 110\rangle_{MgO}$ in $\{0002\}_{Mg}//\{111\}_{MgO}$, as shown in Fig. 7(f). This implies that MgO can serve as heterogeneous nuclei for α-Mg. For the required undercooling, based on the free-growth model [27,28], the critical nucleation undercooling (ΔT_{cn}) is inversely proportional to the particle diameter (d_p), as shown in Eq. (2):

$$\Delta T_{cn}=-\frac{4T_m\gamma_{SL}}{L_v d_p} \quad (2)$$

$$L_v=\lambda\rho \quad (3)$$

Combining Eqs. (2) and (3) above, we have

$$\Delta T_{cn}=-\frac{4T_m\gamma_{SL}}{\rho\lambda d_p} \quad (4)$$

where T_m is the liquidus temperature (K), γ_{SL} is the solid−liquid interface energy (J/m^2), L_v is the latent heat of fusion per unit volume (J/m^3), d_p is the

critical diameter of a particle (m), λ is the specific heat of fusion (J/kg), and ρ is the density (kg/m^3). The thermo-physical parameters of AZ31 Mg alloy obtained from Refs. [29−31] are summarized in Table 2.

Table 2 Thermo-physical parameters of AZ31 Mg alloy [29−31]

Parameter	Value	Ref.
T_m/K	903	[29]
γ_{SL}/(J·m^{-2})	0.115	[30]
λ/(J·kg^{-1})	3.4×10^5	[31]
ρ/(kg·m^{-3})	1780	[29]

Therefore, substituting all the parameters listed in Table 2 into Eq. (4) gives the following Eq. (5):

$$\Delta T_{cn}=\frac{0.686}{d_p} \tag{5}$$

By calculation, the ΔT_{cn} required for MgO_p with an average size of 1.03 μm is approximately 0.6 °C. The related solidification parameters of the alloy, such as $T_{a,N}$ and $T_{\alpha,min}$, can be extracted from the cooling curve (Fig. 11) and are listed in Table 3. The measured maximum ΔT_n is 1.8 °C, which exceeds ΔT_{cn} of 0.6 °C. Therefore, MgO_p is activated as an efficient nucleation site. A previous study [11] concluded that the addition of MgO to pure Mg does not result in grain refinement. However, the HRTEM lattice image indicates that MgO particles can act as the nucleation sites for α-Mg. The reasonable explanation, based on the free-growth model, is that ΔT_n in pure Mg without

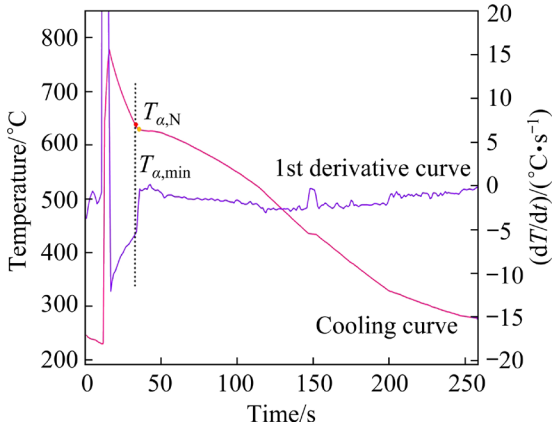

Fig. 11 Cooling curve and related the 1st derivative curve of cast AZ31 Mg alloy with MgO_p addition at 780 °C

Table 3 Related solidification parameters measured from cooling curve

Parameter	Symbol	Value
Nucleation temperature of α-Mg/°C	$T_{\alpha,N}$	628.7
Minimum temperature of α-Mg/°C	$T_{\alpha,min}$	626.9
Nucleation undercooling/°C	ΔT_n	1.8

$\Delta T_n=T_{\alpha,N}-T_{\alpha,min}$

alloying elements is primarily provided by thermal undercooling, which mainly depends on the cooling rate. However, the low thermal undercooling fails to meet ΔT_{cn} required for heterogeneous nucleation, which is closely related to the particle size of the nuclei. Therefore, the grain refinement effect of MgO_p in pure Mg is not consistent with that in the AZ series alloys of this work due to the relatively higher Q value of Al (4.26 °C) and Zn (5.003 °C) [24].

4.2 Grain refinement efficiency influenced by addition temperature of MgO_p

Temperature directly affects the thermo-physical parameters of the alloy melt, including viscosity, density, and surface tension. With increasing temperature, two aspects that affect grain refinement must be considered: melt viscosity and wettability between MgO_p and Mg melt. In terms of melt viscosity, HIRAI [32] conducted a study on the temperature dependence of liquid metal viscosity. The viscosity (η) can be described by the following equations:

$$\eta=A\exp[B/(RT)] \tag{6}$$

$$A=\frac{1.7\times10^{-7}\rho^{2/3}T_m^{1/2}M^{-1/6}}{\exp[B/(RT_m)]} \tag{7}$$

$$B=2.65T_m^{1.27} \tag{8}$$

where T is the liquidus temperature (K), M is the atomic mass (kg/mol), and R is the gas constant (8.3144 J/(mol·K)). GUAN et al [33] established the relationship between the melt density (ρ) of AZ31 Mg alloy and temperature through regression analysis:

$$\rho=-0.1386T+1783.46667 \tag{9}$$

Figure 12(a) displays the relationship between the density/viscosity of the AZ31 Mg alloy melt and

temperature. The density of the AZ31 Mg alloy melt decreases with increasing temperature. In addition, the viscosity of the alloy melt decreases with temperature, resulting in reduced wetting resistance and increased spreadability of the alloy melt on particles [34]. The distribution of particles in the alloy melt is directly affected by the wettability between the particles and the melt. The contact angle can be used to evaluate the wettability between the particles and the melt. According to the Young's equation [35], the contact angle (θ) is defined by the equilibrium relationship of surface tension:

$$\theta = \cos^{-1}\left(\frac{\sigma_{sv}-\sigma_{sl}}{\sigma_{lv}}\right) \quad (10)$$

where σ_{sv}, σ_{sl} and σ_{lv} (N/m) are the interfacial tension of solid−gas, solid−liquid, and liquid−gas, respectively. Temperature affects θ by altering the surface tension σ_{lv}, as indicated by the Eotvos equation [36]:

$$\sigma_{lv}(M/\rho)^{2/3}=K(T_c-T) \quad (11)$$

where T_c is the critical temperature (K) that maintains the maximum temperature of the liquid state; K is a constant of 6.4×10^{-6} J/K for liquid metal. The Eotvos equation reveals that the σ_{lv} of the AZ31 Mg alloy melt decreases with increasing temperature. The values of σ_{lv} in the temperature range applied in this work are depicted in Fig. 12(b). Calculations based on Eqs. (10) and (11) demonstrate that θ decreases as the temperature increases, resulting in improved wettability between MgO_p and the AZ31 Mg alloy melt. This enhanced wettability facilitates the dispersion of MgO_p in the melt.

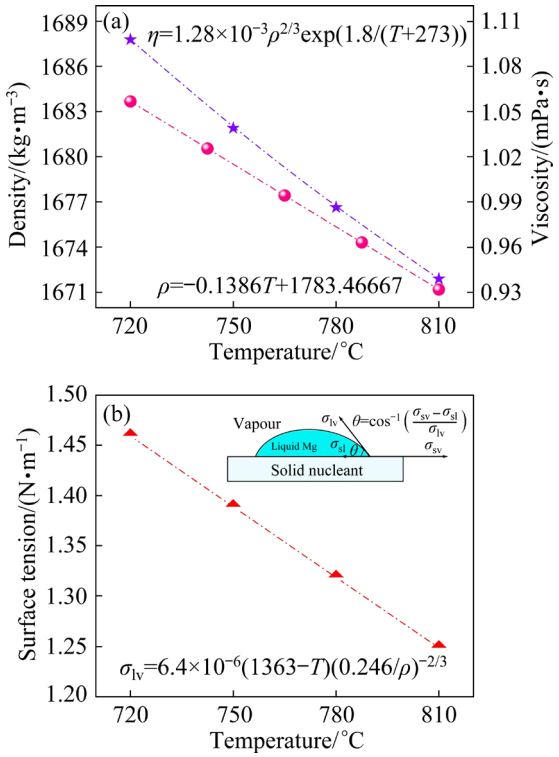

Fig. 12 Thermo-physical properties of AZ31 Mg alloy melt at different temperatures: (a) Viscosity and density; (b) Surface tension

Figure 13 illustrates the mechanism schematics of microstructure evolution in the AZ31 Mg alloy melt. The poor wettability between MgO_p and Mg melt at a lower temperature of 720 °C results in the undesirable agglomeration of MgO_p. As the addition temperature increases, the dispersion of MgO_p is promoted, resulting in a better grain refinement effect. However, the density is decreased to a minimum value (1.67 g/cm^3) at the highest addition temperature of 810 °C, leading to serious settlement of the MgO_p and deterioration of grain refinement.

4.3 Strengthening mechanism

The increase in YS of the cast AZ series alloy with MgO_p addition could be attributed to the following reasons: (1) grain refinement strengthening ($\Delta\sigma_{GR}$), (2) Orowan strengthening $\Delta\sigma_{Orowan}$, and (3) load transfer strengthening ($\Delta\sigma_{LT}$), as reported in previous literature [37−39]. Therefore, adding those strengthened contributions presented above, the theoretical contribution to YS ($\Delta\sigma_{theoretic}$) can be calculated as follows:

$$\Delta\sigma_{theoretic}=\Delta\sigma_{GR}+\Delta\sigma_{Orowan}+\Delta\sigma_{LT} \quad (12)$$

$\Delta\sigma_{GR}$ can be estimated by the Hall−Petch relationship [40]:

$$\Delta\sigma_{GR}=k(d_i^{-1/2}-d_0^{-1/2}) \quad (13)$$

where k is the stress concentration factor estimated to be 257.3 MPa·μm$^{1/2}$ for cast AZ31 Mg alloy [41], d_0 and d_i represent the average grain size of untreated AZ31 Mg alloy and AZ31 Mg alloy with MgO_p addition at different temperatures (750, 780, and 810 °C), respectively. $\Delta\sigma_{GR}$ for the cast AZ31 Mg alloys with MgO_p addition at 750, 780, and 810 °C can be calculated to be 3.7, 9.3 and 7.1 MPa, respectively. $\Delta\sigma_{Orowan}$ and $\Delta\sigma_{LT}$ can be calculated as follows [38]:

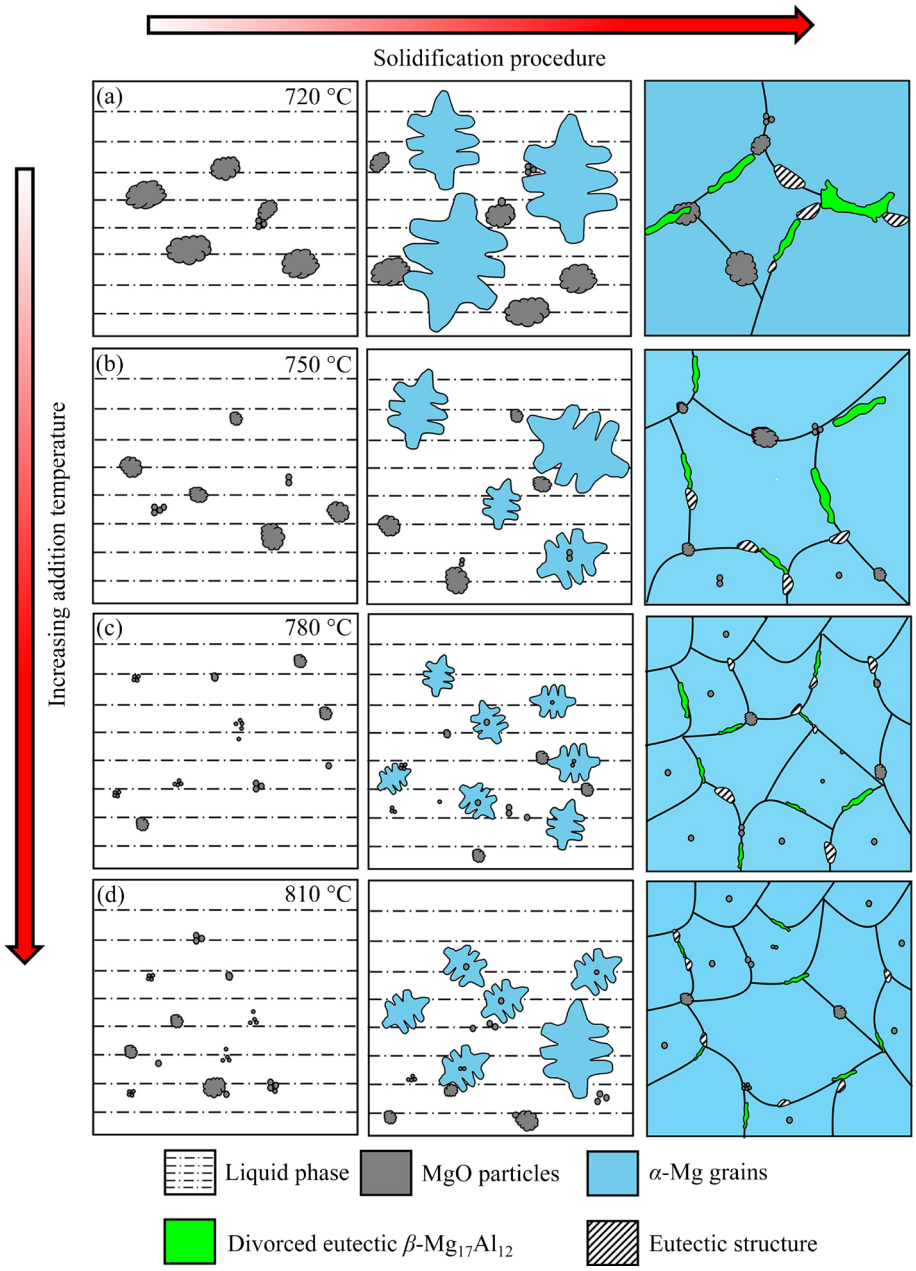

Fig. 13 Schematic diagrams of microstructure evolution during solidification at different MgO_p addition temperatures: (a) 720 °C; (b) 750 °C; (c) 780 °C; (d) 810 °C

$$\Delta\sigma_{\text{Orowan}} = 0.8GMb\sqrt{\frac{2f_v}{\pi d^2}} \tag{14}$$

$$\Delta\sigma_{\text{LT}} = \frac{f_v\sigma_m}{2} \tag{15}$$

where b and G are the amplitude of Burgers vector (3.21×10^{-10} m) and shear modulus (1.58×10^4 MPa) of the Mg matrix, respectively [38], M denotes the Taylor factor (3.0), f_v is the volume fraction of the MgO (0.6%), d is the average diameter of the MgO (1.03 μm), and σ_m is the YS of the untreated AZ31 Mg alloy (44.8 MPa). By calculation, $\Delta\sigma_{\text{Orowan}}$ and $\Delta\sigma_{\text{LT}}$ are determined to be 7.3 and 13.4 MPa, respectively. Therefore, $\Delta\sigma_{\text{theoretic}}$ of the cast AZ31 Mg alloys with MgO_p addition at 750, 780 and 810 °C is 24.4, 30 and 27.8 MPa, respectively. However, the tensile properties show that the actual YS of the samples with MgO_p addition at 750,780 and 810 °C is 5, 16 and 11.9 MPa higher than that of the untreated AZ31 Mg alloy, respectively. These findings indicate that the actual contribution to YS is lower than the theoretical value as shown in Fig. 14. This discrepancy can be attributed to the fact that the theoretical calculations are based on the

ideal state of uniformly distributed MgO_p, and it is difficult to ensure that MgO_p is uniformly distributed in the actual preparation process. Moreover, it can be found in Fig. 14 that the actual contribution to YS at the addition temperature of 780 °C is the closest to the theoretical value, which provides evidence of a more uniform distribution of MgO_p at this temperature.

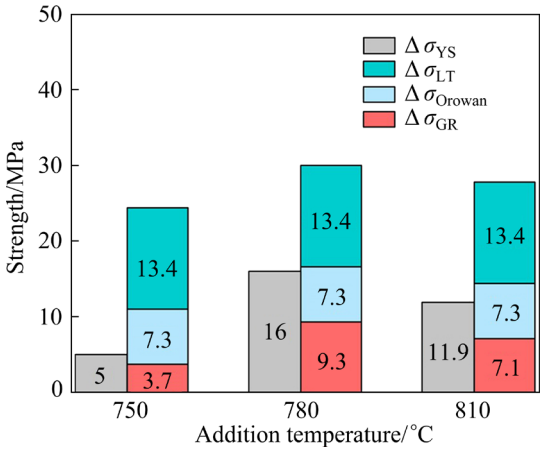

Fig. 14 Actual YS contribution and theoretical YS contribution of cast AZ31 Mg alloys with MgO_p addition at 750, 780 and 810 °C

5 Conclusions

(1) As the MgO_p addition temperature increases from 720 to 810 °C, the grain size of the AZ31 Mg alloy first decreases and then increases, exhibiting a minimum value of 136 μm at 780 °C.

(2) The grain refinement is mainly due to the heterogeneous nucleation induced by MgO with the potential orientation of $\langle 11\bar{2}0\rangle Mg // \langle 01\bar{1}\rangle MgO$ in $\{0002\}_{Mg}//\{111\}_{MgO}$ according to the HRTEM observation at the interface of Mg/MgO, which verifies the excellent interfacial bonding.

(3) The improved grain refinement efficiency with increasing MgO_p addition temperature can be attributed to the reduced melt viscosity and enhanced wettability between MgO_p and the Mg melt.

(4) The theoretical contribution of grain refinement strengthening, Orowan strengthening, and load transfer strengthening to the yield strength of the sample with MgO_p addition at 780 °C are 7.8, 13.4 and 23.5 MPa, respectively. However, the actual increase of yield strength is lower than the theoretical value, which is attributed to the uneven distribution of MgO_p.

CRediT authorship contribution statement

Le ZAI: Methodology, Investigation, Data curation, Formal analysis, Writing – Original draft; **Xin TONG:** Investigation, Formal analysis; **Yun WANG:** Writing – Review & editing; **Xiao-huai XUE:** Supervision, Funding acquisition.

Declaration of competing interest

The authors declare that they have no known competing financial interests or personal relationships that could have appeared to influence the work reported in this paper.

Acknowledgments

This work was supported by the National Natural Science Foundation of China (No. 51871155).

References

[1] WANG Yin-xin, ZENG Xiao-qin, DING Wen-jiang, LUO A A, SACHDEV A K. Grain refinement of AZ31 magnesium alloy by titanium and low-frequency electromagnetic casting [J]. Metallurgical and Materials Transactions A, 2007, 38: 1358−1366.

[2] CHENG Ren-ju, PAN Fu-sheng, JIANG Shan, LI Cheng, JIANG Bin, JIANG Xian-quan. Effect of Sr addition on the grain refinement of AZ31 magnesium alloys [J]. Progress in Natural Science: Materials International, 2013, 23(1): 7−12.

[3] DU Jun, WANG Ming-hua, ZHOU Ming-chuan, LI Wen-fang. Evolutions of grain size and nucleating particles in carbon-inoculated Mg−3%Al alloy [J]. Journal of Alloys and Compounds, 2014, 592: 313−318.

[4] SURESH M, SRINIVASAN A, PILLAI U T S, PAI B C. The effect of charcoal addition on the grain refinement and ageing response of magnesium alloy AZ91 [J]. Materials Science and Engineering A, 2011, 528(29/30): 8573−8578.

[5] TONG Xin, YOU Guo-qiang, LIU Yan, LONG Si-yuan, LIU Qing. Effect of C_2H_2 as a novel gas inoculant on the microstructure and mechanical properties of as-cast AM60B magnesium alloy [J]. Journal of Materials Processing Technology, 2019, 271: 271−283.

[6] HAN Meng-xia, ZHU Xiang-zhen, GAO Tong, LIU Xiang-fa. Revealing the roles of Al_4C_3 and Al_8Mn_5 during α-Mg nucleation in Mg−Al based alloys [J]. Journal of Alloys and Compounds, 2017, 705: 14−21.

[7] LIAO Heng-bin, MO Li-ling, LI Cheng-bo, ZHAN Mei-yan, DU Jun. Grain refinement of Mg−Al binary alloys inoculated by in-situ oxidation[J]. Transactions of Nonferrous Metals Society of China, 2022, 32(10): 3212−3221.

[8] ALI Y, QIU Dong, JIANG Bin PAN Fu-sheng, ZHANG Ming-xing. The influence of CaO addition on grain refinement of cast magnesium alloys [J]. Scripta Materialia, 2016, 114: 103−107.

[9] ZHAO Jia, YOU Chen, CHEN Ming-fang, LYU Shao-yuan, TIE Di, LIU Hai-feng. Effect of calcium oxide particle size

on microstructure and properties of AZ91 Mg alloy [J]. Journal of Alloys and Compounds, 2021, 886: 160970.

[10] PENG Guo-sheng, WANG Yun, FAN Zhong-yun. Competitive heterogeneous nucleation between Zr and MgO particles in commercial purity magnesium [J]. Metallurgical and Materials Transactions A, 2018, 49: 2182−2192.

[11] MA Zhi-qiang, LI Cheng-bo, DU Jun, ZHAN Mei-yan. Grain refinement of Mg−Al alloys inoculated by MgO powder [J]. International Journal of Metalcasting, 2019, 13: 674−685.

[12] FAN Zhong-yun, WANG Yun, XIA Ming-xu, ARUMUGANATHAR S. Enhanced heterogeneous nucleation in AZ91D alloy by intensive melt shearing [J]. Acta Materialia, 2009, 57(16): 4891−4901.

[13] ZHANG Li-li, JIANG Hong-xiang, HE Jie, ZHAO Jiu-zhou. Kinetic behaviour of TiB2 particles in Al melt and their effect on grain refinement of aluminium alloys [J]. Transactions of Nonferrous Metals Society of China, 2020, 30(8): 2035−2044.

[14] HASHIM J, LOONEY L, HASHMI M S J. Particle distribution in cast metal matrix composites—Part I [J]. Journal of Materials Processing Technology, 2002, 123(2): 251−257.

[15] KUMAR S, SUMAN K N S, RAVINDRA K, PODDAR P, SIVA V. Microstructure, mechanical response and fractography of AZ91E/Al_2O_3 (p) nano composite fabricated by semi solid stir casting method [J]. Journal of Magnesium and Alloys, 2017, 5(1): 48−55.

[16] ABDIZADEH H, BAHARVANDI H R, MOGHADDAM K S. Comparing the effect of processing temperature on microstructure and mechanical behavior of ($ZrSiO_4$ or TiB_2)/ aluminum composites [J]. Materials Science and Engineering A, 2008, 498(1/2): 53−58.

[17] SOLTANI S, KHOSROSHAHI R A, MOUSAVIAN R T, JIANG Zheng-yi, BOOSTANI A F, BRABAZON D. Stir casting process for manufacture of Al−SiC composites [J]. Rare Metals, 2017, 36: 581−590.

[18] ABDIZADEH H, EBRAHIMIFARD R, BAGHCHESARA M A. Investigation of microstructure and mechanical properties of nano MgO reinforced Al composites manufactured by stir casting and powder metallurgy methods: A comparative study [J]. Composites Part B: Engineering, 2014, 56: 217−221.

[19] LAURENT V, JARRY P, REGAZZONI G, APELIAN D. Processing-microstructure relationships in compocast magnesium/SiC [J]. Journal of Materials Science, 1992, 27: 4447−4459.

[20] QIU Dong, ZHANG Ming-xing. The nucleation crystallography and wettability of Mg grains on active Al_2Y inoculants in an Mg−10wt.%Y alloy [J]. Journal of Alloys and Compounds, 2014, 586: 39−44.

[21] LIAO Heng-bin, MO Li-ling, ZHOY Xiong, ZHAO Bing, DU Jun. Grain refinement and improvement of mechanical properties of AZ31 magnesium alloy inoculated by in-situ oxidation process [J]. Journal of Materials Research and Technology, 2021, 12: 807−817.

[22] WANG Yun, FAN Zhong-yun, ZHOU Xiao-rong, THOMPSON G E. Characterisation of magnesium oxide and its interface with α-Mg in Mg−Al-based alloys [J]. Philosophical Magazine Letters, 2011, 91(8): 516−529.

[23] AVEDESIAN M M, BAKER H. Magnesium and magnesium alloys [M]//ASM specialty handbook. Ohio: The Materials Information Society, 1999: 52.

[24] ALI Y, QIU Dong, JIANG Bin, PAN Fu-sheng, ZHANG Ming-xing. Current research progress in grain refinement of cast magnesium alloys: A review article [J]. Journal of Alloys and Compounds, 2015, 619: 639−651.

[25] STJOHN D H, QIAN Ma, EASTON M A, CAO Peng, HILDEBRAND Z. Grain refinement of magnesium alloys [J]. Metallurgical and Materials Transactions A, 2005, 36: 1669−1679.

[26] STJOHN D H, EASTON M A, QIAN Ma, TAYLOR J A. Grain refinement of magnesium alloys: A review of recent research, theoretical developments, and their application [J]. Metallurgical and Materials Transactions A, 2013, 44: 2935−2949.

[27] GREER A L, BUNN A M, TRONCHE A, EVANS P V, BRISTOW D J. Modelling of inoculation of metallic melts: Application to grain refinement of aluminium by Al−Ti−B [J]. Acta Materialia, 2000, 48(11): 2823−2835.

[28] TONG Xin, WU Guo-hua, EASTON M A, SUN Ming, STJOHN D H, JIANG Rui, QI Fang-zhou. Exceptional grain refinement of Mg−Zr master alloy treated by tungsten inert gas arc re-melting with ultra-high frequency pulses [J]. Scripta Materialia, 2022, 215: 114700.

[29] HASAN M, BEGUM L. On numerical modeling of low-head direct chill ingot caster for magnesium alloy AZ31 [J]. Journal of Magnesium and Alloys, 2014, 2(4): 275−286.

[30] MONTIEL D, LIU Li-ming, XIAO Li-yuan, PROVATAS N. Microstructure analysis of AZ31 magnesium alloy welds using phase-field models [J]. Acta Materialia, 2012, 60(16): 5925−5932.

[31] HADADZADEH A, WELLS M A. Mathematical modeling of thermo-mechanical behavior of strip during twin roll casting of an AZ31 magnesium alloy [J]. Journal of Magnesium and Alloys, 2013, 1(2): 101−114.

[32] HIRAI M. Estimation of viscosities of liquid alloys [J]. ISIJ International, 1993, 33(2): 251−258.

[33] GUAN Ren-guo, ZHAO Zhan-yong, CHEN Li-qing, WANG Fu-xing, Numerical simulation of continuous rheo-extrusion process of AZ31 Mg alloy [J]. The Chinese Journal of Nonferrous Metals, 2010, 20(5): 924−929. (in Chinese)

[34] LANDRY K, EUSTATHOPOULOS N. Dynamics of wetting in reactive metal/ceramic systems: Linear spreading [J]. Acta Materialia, 1996, 44(10): 3923−3932.

[35] SEVENO D, BLAKE T D, De CONINCK J. Young's equation at the nanoscale [J]. Physical review letters, 2013, 111(9): 096101.

[36] SHERESHEFSKY J L. Surface tension of saturated vapors and the equation of Eötvös [J]. The Journal of Physical Chemistry, 2002, 35(6): 1712−1720.

[37] ZHANG Zhen-ya, GUO Yu-hang, ZHAO Yu-tao, CHEN Gang, WU Ji-li, LIU Man-ping. Effect of reinforcement spatial distribution on mechanical properties of MgO/ZK60 nanocomposites by powder metallurgy [J]. Materials Characterization, 2019, 150: 229−235.

[38] YUAN Qiu-hong, QIU Zhi-qiang, ZHOU Guo-hua, ZENG Xiao-shu, LUO Lan, RAO Xi-xin, DING Yan, LIU Yong.

Interfacial design and strengthening mechanisms of AZ91 alloy reinforced with in-situ reduced graphene oxide [J]. Materials Characterization, 2018, 138: 215−228.
[39] YUAN Qiu-hong, ZENG Xiao-shu, LIU Yong, LUO Lei, WU Jun-bin, WANG Yan-chun, ZHOU Guo-hua. Microstructure and mechanical properties of AZ91 alloy reinforced by carbon nanotubes coated with MgO [J]. Carbon, 2016, 96: 843−855.
[40] TONG Xin, WU Guo-hua, ZHANG Liang, LIU Wen-cai, DING Wen-jiang. Achieving low-temperature Zr alloying for microstructural refinement of sand-cast Mg−Gd−Y alloy by employing zirconium tetrachloride [J]. Materials Characterization, 2021, 171: 110727.
[41] QIU Wei, LIU Zhi-qiang, YU Rong-zong, CHRN Jian, REN Yan-jie, HE Jian-jun, LI Wei, LI Cong. Utilization of VN particles for grain refinement and mechanical properties of AZ31 magnesium alloy [J]. Journal of Alloys and Compounds, 2019, 781: 1150−1158.

添加温度对 MgO 在镁合金中分散行为及晶粒细化效率的影响

宰 乐[1]，童 鑫[1]，王 云[2]，薛小怀[1]

1. 上海交通大学 材料科学与工程学院，上海 200240；
2. Brunel Centre for Advanced Solidification Technology (BCAST), Brunel University London, Uxbridge, Middlesex UB8 3PH, United Kingdom

摘 要：研究 MgO 颗粒的添加温度对其在 AZ31 镁合金中的分散行为和晶粒细化效率的影响。通过组织表征、热力学计算和凝固曲线分析，系统研究晶粒细化机制。结果表明，随着 MgO 添加温度从 720 ℃升高到 810 ℃，AZ31 镁合金的晶粒尺寸先减小后增大，在 780 ℃时达到最小值 136 μm；随着 MgO 添加温度的升高，晶粒细化效率提高，这归因于 Mg 熔体黏度的降低以及 MgO 颗粒与 Mg 熔体之间润湿性的改善。此外，提出了描述凝固行为和晶粒细化机理的物理模型。

关键词：晶粒细化；MgO 形核颗粒；AZ31 镁合金；添加温度；分散行为

(Edited by Xiang-qun LI)